Rediscovering Wet Ball Grinding Physics for Material Production Optimization: Symbolic Regression on Experimental and Neural Network-Augmented CFD-DEM Data

Ahmed Eisa[1*], Mayank Gupta[2], Christoph Thon[1], Tilmann Joerren[1], Bakytzhan Konratov[1], Somayeh Hosseinhashemi[1], Oliver Pikhard[3] and Carsten Schilde[1]

[1*] Institute for Particle Technology, Technical University of Braunschweig,
Volkmaroder Str. 5, Brunswick, 38108, Lower Saxony, Germany.
ahmed.eisa@tu-braunschweig.de; c.thon@tu-braunschweig.de;
t.joerren@tu-braunschweig.de; b.konratov@tu-braunschweig.de;
s.hosseinhashemi@tu-braunschweig.de; c.schilde@tu-braunschweig.de
[2] Indian Institute of Technology Bombay,
Academic Section, IIT Area, Mumbai, 400076, Maharashtra, India.
210101002@iitb.ac.in
[3] Materials Production, BASF SE, Carl-Bosch-Str. 38, Ludwigshafen,
67056, Ludwigshafen am Rhein, Germany.
oliver.pikhard@basf.com

Abstract. This study integrates Computational Fluid Dynamics–Discrete Element Method (CFD–DEM) simulations with symbolic regression to develop interpretable models for wet ball grinding. A Neural Network (NN) based extrapolation bridges the computational–experimental scale gap, enabling simulations at tractable particle sizes (755–2000 μm) to inform models for industrially relevant sizes (214–800 μm). Six symbolic regression frameworks were rigorously benchmarked: mainstream methods PySR and gplearn; PhySO; the physics-informed framework SyBReN; classic Simulated Annealing (SA); and a novel Simulated Annealing–Markov-Chain (SA-MC) approach introduced in this work and released as open-source software. The analysis successfully reconstructed key components of Kwade's energy model directly from data without theoretical constraints. Using simulation-derived stress parameters, predictions of experimental specific energy achieved coefficients of determination $R^2 > 0.9$, demonstrating that physics-informed computational features can reliably forecast real grinding performance. SA-MC delivered robust performance across equation complexities while avoiding complete failures, relying only on experimentally accessible parameters. The discovered expressions reveal previously hidden grinding mechanics, providing transparent and physically meaningful equations suitable for real-time process control and establishing foundations for future digital twin implementation in industrial comminution.

Keywords: Symbolic Regression, Wet Ball Grinding, CFD-DEM Simulation, Neural Network Extrapolation, Process Optimization, Interpretable Machine Learning, Digital Twin

1 Introduction

Comminution occupies a paradoxical position in process industries: indispensable for mineral liberation, pigment dispersion, pharmaceutical formulations, and high-performance ceramics production, yet notoriously energy-intensive, often consuming the largest fraction of plant electricity. For over a century, researchers have sought predictive models for optimization, scale-up, and control.

The earliest attempts were classical energy laws formalizing the relationship between grinding energy and particle size reduction. Rittinger argued that energy required for comminution is proportional to surface area increase [1], while Kick countered that fracture energy should scale with volume reduction [2]. Bond introduced his "third theory," interpolating between the two and remaining a cornerstone of industrial mill design [3]. Hukki later emphasized that no single theory is universally valid, proposing a "solomonic settlement" accounting for different particle size ranges [4]. Meloy attempted to unify these perspectives through dimensional analysis in a physically consistent framework [5]. These works shaped practice for decades and framed scientific debate around energy efficiency.

By the mid-20th century, comminution science shifted to more mechanistic formulations. Austin, Klimpel, and Luckie developed detailed ball milling treatments [6]. Herbst and Fuerstenau demonstrated control strategies rooted in breakage kinetics [7]. Napier-Munn's monograph brought together decades of plant experience [8], while King emphasized simulation as a design tool [9]. Population Balance Models (PBMs) became central, with Hinde et al. [10] demonstrating their use for predicting product distributions, and Austin and Bagga providing fundamental analyses [11]. PBMs offered elegance and predictive rigor but remained difficult to calibrate, limiting day-to-day plant application.

A new perspective arose through Kwade's stress intensity/stress number model. Kwade [12] framed wet comminution in stirred mills using two key parameters: Stress Intensity (SI) [Pa] and Number of Stress Events (SN) [-]. Subsequent work by Kwade and Schwedes [13] examined material breakage characteristics, while later studies provided design guidelines for nanoparticle production [14], validated particle size distribution predictions [15], investigated stirred media mills [16,17], analyzed energy efficiency [18], and considered industrial scale-up [19]. This mechanistic-empirical framework remains influential in laboratory and industrial practice.

Despite these advances, semi-empirical model limitations persisted. They often required material-specific calibration and could not capture nonlinear interactions involving slurry rheology, particle-particle effects, or wear. Janković et al. [20] underscored cement grinding optimization challenges, Napier-Munn et al. [21] highlighted gaps in linking design to circuit performance, and Cho et al. [22] emphasized ball sizing optimization importance.

The advent of DEM and CFD fundamentally expanded the comminution modeling toolbox. Cundall and Strack [23] introduced DEM for granular assemblies, extended by Tsuji et al. [24] to fluid-particle flows. Reviews by Deen et al. [25] and Zhu et al. [26] documented rapid spread. Cleary [27] pioneered DEM in grinding, followed by Sinnott, Cleary and Morrison [28,29], Weerasekara et al. [30], and Powell et al. [31]. Coupled CFD-DEM methods matured with Suzzi et al. [32], Radeke et al. [33], and Mori et al. [34], while comprehensive models emerged from Radl et al. [35] and Herbst et al. [36]. Recent applications include Sinnott et al. [37], Mayank et al. [38], Cleary and Owen [39], Larsson et al. [40], Fragnière et al. [41], and Tanneru et al. [42]. These high-fidelity simulations provided unprecedented detail but computational cost limited routine industrial deployment.

To overcome this bottleneck, researchers increasingly turned to NN augmentation of simulation data. Raissi et al. [43] introduced Physics-Informed Neural Networks (PINNs), while Han et al. [44] demonstrated deep networks for high-dimensional PDEs. Thuerey et al. [45] applied deep learning to accelerate flow prediction, and Meng et al. [46] showed NNs can approximate DEM outcomes for granular flows. Such methods enable extrapolating simulation results into experimental parameter ranges, yielding hybrid datasets combining CFD-DEM accuracy with machine learning flexibility.

The resulting gap is striking: plants collect extensive data—power draw, torque, slurry density, particle size distributions—yet converting these into actionable predictive models remains difficult. Black-box machine learning has been trialed, but its lack of transparency makes adoption unlikely in safety-critical and regulated industries. Interpretability is essential: engineers need not just predictions but understanding of why variables matter.

Here, Symbolic Regression (SR) presents a compelling solution. SR searches mathematical expression space to find formulas fitting data while remaining interpretable. Schmidt and Lipson's seminal work [47] demonstrated SR could rediscover physical laws directly from experimental data. Modern frameworks balance computational performance and interpretability differently: PySR provides evolutionary search with gradient refinement [48]; gplearn implements genetic programming in Python [49]; PhySO integrates physics-inspired priors and dimensional constraints [50]; SyBReN applies physics-inspired modeling in industrial contexts [51].

In parallel, stochastic optimization strategies contributed to SR evolution. SA, introduced by Kirkpatrick et al. [52] and independently by Černý [53], uses thermodynamic analogies to escape local minima. Its theoretical grounding lies in Markov Chains (MC), developed by Markov [54] and extended by Harchol-Balter [55]. Liang et al. [56] combined genetic programming with Markov Chain Monte Carlo (MCMC) for symbolic regression, framing equation discovery as stochastic sampling guided by Bayesian inference. Building on these ideas, we introduce SA-MC, a simulated annealing-Markov chain variant tailored to noisy, moderate-scale datasets typical of comminution experiments.

Beyond algorithmic diversity, SR aligns with the push toward interpretable machine learning. Rudin [57] argues against deploying black-box models in high-stakes decisions. Molnar [58] systematizes interpretability methods, while Lipton [59] critiques interpretability misconceptions, and Doshi-Velez and Kim [60] call for rigorous explanation science. In process engineering, these principles are critical: operators must trust models influencing production. Bangi et al. [61] emphasize hybrid modeling, showing how mechanistic and data-driven approaches combine. SR naturally supports this paradigm by rediscovering mechanistic terms while remaining flexible to empirical data.

The implications for comminution are significant. Transparent symbolic models enable optimization with respect to any key performance indicator while remaining interpretable. They can act as soft sensors predicting target metrics in real time, reducing reliance on costly measurements and enabling control loop integration for automated monitoring, quality stabilization, and operational efficiency improvement.

This paper presents precisely such a workflow. Laboratory grinding experiments and CFD-DEM simulations combine into a hybrid dataset, augmented by NN extrapolations, covering torque, Particle Size Distributions (PSDs), slurry metrics, stirrer speeds, and bead sizes. This dataset benchmarks SR frameworks: PySR, gplearn, PhySO, SyBReN, and SA, against the newly developed SA-MC method. SA-MC balances exploration and parsimony, producing compact, physically meaningful models. Figure 1 summarizes the complete pipeline, illustrating how experimental and computational data are integrated through symbolic regression frameworks to produce transparent equations for process optimization.

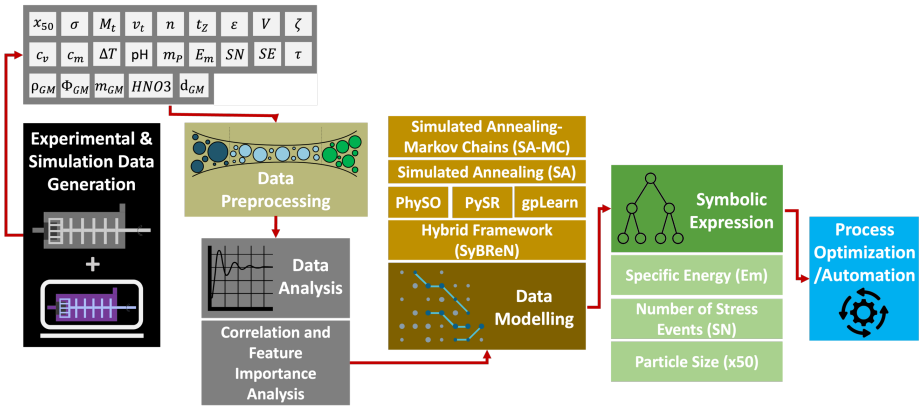

Fig. 1. Workflow for developing interpretable comminution models: experimental and CFD–DEM data are combined, analyzed, and modeled with symbolic regression frameworks (PySR, gplearn, PhySO, SyBReN, SA, SA-MC) to produce transparent equations for optimization and soft sensing.

Our contribution unfolds along four dimensions. First, we generate and process a comprehensive dataset combining laboratory grinding experiments with CFD-DEM simulations to capture parameters otherwise inaccessible experimentally. Second, we augment simulation data with neural-network extrapolation to bridge the gap between tractable computational bead sizes and experimentally feasible ranges, enabling hybrid datasets suitable for modeling. Third, we develop SA-MC, a novel SR method grounded in simulated annealing and Markov chain theory. Fourth, we benchmark SA-MC against leading SR frameworks, establishing a reproducible evaluation framework for comminution modeling. Finally, in the Outlook, we outline how transparent, equation-based models could be deployed to improve grinding efficiency in industrial contexts. Collectively, these contributions advance interpretable, data-driven process optimization and bridge the divide between mechanistic comminution models and black-box machine learning.

2 Methodology

2.1 Experimental Setup and Data Acquisition

To develop a robust dataset for accurately modeling key process parameters in wet stirred media milling systems, experimental data were obtained from the PML V-H laboratory bead mill. The PML V-H is a 1.2-liter, 3.3 KW stirred media mill manufactured by Draiswerke (now Bühler Group) in 1991, representing a well-characterized laboratory-scale grinding system suitable for fundamental process investigation, providing precise control over grinding conditions while enabling comprehensive process monitoring and data collection.

Figure 2 demonstrates the mill configuration and the complex temporal evolution of three key process parameters during grinding operations. The mill features a horizontal Wet Stirred Media Mill design with sophisticated monitoring capabilities that enable real-time tracking of the Suspension Conductivity (σ) [µS/cm] and Torque on the Shaft (M_t) [Nm] throughout the grinding process. The Median Particle Size (x_{50}) [µm], was determined by periodically withdrawing samples at defined time intervals, which were subsequently analyzed offline to quantify the median particle size evolution.

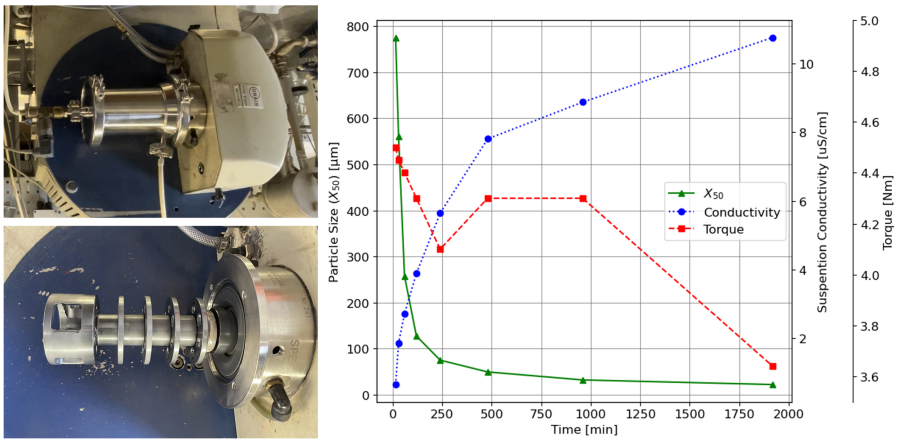

Fig. 2. PML V-H mill configuration showing rotor assembly with grinding discs (left) and temporal evolution of x_{50} , σ , and M_t during 5-hour grinding operation (right)

The experimental campaign focused on aluminum oxide processing using steel grinding beads with diameters ranging from 214 to 800 µm, representing the fine grinding regime typical of industrial applications. This size range encompasses both the transition from impact-dominated to attrition-dominated breakage mechanisms and provides sufficient variation for comprehensive model development. The selection of steel grinding media ensured consistent material properties characterized by high density (7850 kg/m³) and mechanical strength, avoiding potential contamination issues that might arise with ceramic alternatives. In total, the dataset comprised 20 experimental runs, covering the full range of grinding media sizes and operating conditions considered in this study.

The experimental matrix encompassed Circumferential Speed (v_t) [m/s] varying systematically between 6 and 12 m/s, corresponding to different energy input levels and stress intensities within the mill. These velocity ranges were selected to cover the operational envelope typical of industrial wet grinding applications while maintaining sufficient energy input for effective particle breakage. Solid content levels were systematically adjusted from 10% to 30% by volume to investigate the influence of suspension concentration on grinding efficiency and energy utilization.

All experimental runs were conducted over approximately 5 hours to ensure sufficient process evolution and statistical significance of measurements. As demonstrated in Figure 2, the temporal evolution shows characteristic grinding behavior with initial rapid x_{50} reduction from approximately 780 µm to below 100 µm, followed by gradual stabilization. Simultaneously, σ increases systematically due to increased particle surface area and potential contamination, while M_t initially decreases as particle breakage reduces grinding resistance, then stabilizes at steady-state conditions.

Process Parameter Measurement. During each experimental run, comprehensive process monitoring was implemented through discrete time interval measurements, with sampling frequencies optimized to capture both rapid transient phenomena and long-term process evolution. Key parameters included as mentioned previously the Particle Size Distribution (PSD) evolution, measured using laser diffraction techniques to track the progression of particle breakage throughout the grinding process. M_t on the main shaft was continuously recorded using precision torque sensors, enabling real-time monitoring of power consumption and stress conditions within the mill. In addition, a broad set of process parameters was systematically recorded to characterize the mechanical and operational state of the system. These included v_t, Grinding Time (t_Z) [s], particle size (x_{10}, x_{50}, x_{90}), Specific Energy (E_m) [J/kg], Stirrer Speed (n) [rad/s], Porosity(ε) [-], Grinding Media Diameter (d_{GM}) [µm], Grinding Media Density (ρ_{GM}) [kg/m^3] and Media Filling Rate (Φ_{GM}) [-].

To capture suspension behavior and material transport, further parameters included Grinding Media Mass (m_{GM}) [kg], Product Mass (m_P) [kg], Volume Concentration (c_v) [-], Mass Concentration (c_m) [-], and Volume Flow through the mill (V) [m^3/s]. The physicochemical state of the suspension was characterized was characterized by Temperature Difference between Mill Inlet and Outlet (ΔT) [°C], Zeta Potential (ζ) [mV], pH Value (pH) [-], σ , and the Amount of Nitric Acid ($HNO3$) [mol/L].

This holistic measurement framework ensured that the mechanical, operational, and physicochemical aspects of the grinding process were comprehensively captured, providing a detailed basis for analyzing its relationship to particle size reduction, process efficiency, and suspension stability.

Thermal monitoring encompassed inlet and outlet fluid temperatures to quantify heat generation and potential thermal effects on suspension properties. pH values were systematically tracked to monitor potential chemical interactions between the grinding media, aluminum oxide particles, and process fluid. Electrical conductivity measurements provided additional insights into suspension chemistry and potential contamination effects, as clearly demonstrated by the systematic conductivity increase shown in Figure 1.

The E_m values were directly measured during experimental operations, providing precise quantification of energy input per unit mass of processed material and enabling direct comparison with the milling system's developed CFD-DEM Method simulation-based generated E_m data. The E_m represents the energy required to grind or process a material, normalized per unit mass, serving as a critical parameter for quantifying the efficiency of energy utilization during material processing. These measured Em values formed the primary validation targets for subsequent model development.

Validation Framework and Benchmark Models. The experimental framework was designed to enable validation against the established stress-energy model proposed by

Kwade, which provides a fundamental framework for understanding grinding processes in stirred media mills. Kwade's model is grounded in stress-energy principles, elucidating the relationship between the Intensity, Frequency and Energy of stress events in a stirred media mill and their effect on particle comminution. The model incorporates both the SN and the SE as critical variables, with these parameters influenced by multiple process variables including d_{GM}, ρ_{GM}, n, v_t, t_Z , ε and Φ_{GM}.

The SE component of Kwade's model incorporates a linear relationship with m_{GM} and a quadratic dependence on vt, scaled by an empirical factor that accounts for media properties. In parallel, the SN calculation integrates geometric and operational parameters to quantify the frequency of particle–media interactions. Together, this theoretical framework enables precise prediction of the energy demands for material size reduction, with its main value lying in its scalability and precision for optimizing industrial grinding operations and improving energy efficiency.

2.2 CFD-DEM Method Simulations

Simulation Framework and Software Implementation. To complement experimental observations and extract process parameters not accessible through experimental measurements alone, two-way coupled CFD-DEM simulations were implemented using Rocky DEM and Fluent CFD software packages from Ansys. This integrated approach enabled detailed analysis of SE distributions, Shear Stress (τ) [Pa] fields, and dynamic particle interactions within the mill geometry at a level of detail impossible to achieve through experimental measurements alone.

The comprehensive workflow for establishing and executing the coupled CFD-DEM simulations is illustrated in Figure 3, which demonstrates the systematic approach required for successful integration of the two computational domains. The workflow encompasses geometry preparation, mesh generation, boundary condition specification, and iterative coupling procedures that ensure accurate representation of the complex fluid-particle interactions occurring within the grinding environment.

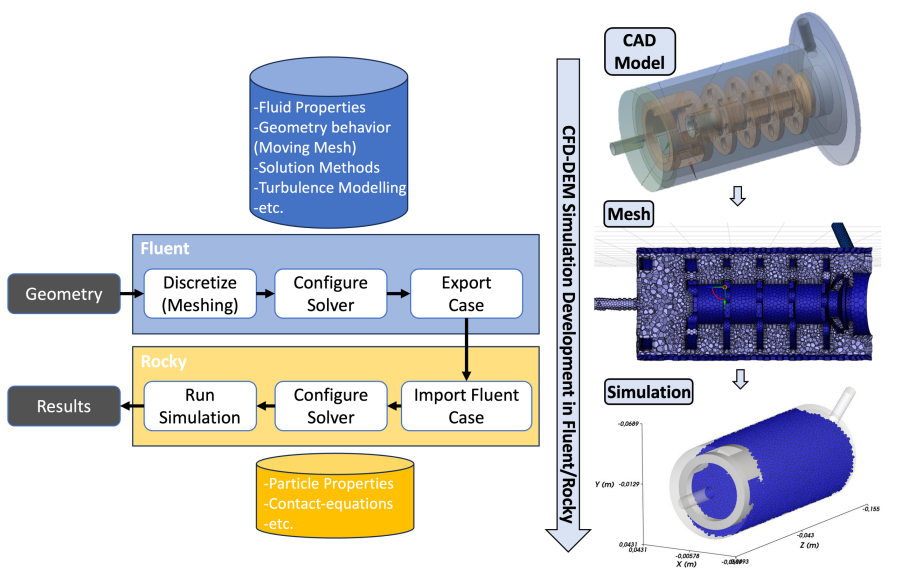

Fig. 3. Comprehensive CFD-DEM simulation workflow showing the integration of Rocky DEM and Fluent CFD with CAD geometry preparation, mesh generation, and final simulation results including particle dynamics visualization

The CFD-DEM methodology represents a sophisticated computational approach where fluid flow and particle dynamics are simultaneously solved with full coupling between phases. The CFD component employs finite volume discretization to solve the governing fluid flow equations, while the DEM component tracks individual particle trajectories and collision dynamics. The two-way coupling ensures that particles influence fluid flow through momentum exchange, while fluid forces affect particle motion, creating a comprehensive representation of the grinding environment.

Geometry Modeling and Mesh Generation. The geometry modeling accurately represented the PML V-H mill configuration based on detailed engineering drawings, including precise stirrer pin dimensions, spacing, and angular orientations. The rotor assembly consisted of four grinding discs (70 mm diameter, 5 mm thickness) and one stirrer head (43 mm height), with 19 mm spacing between adjacent discs, creating a total rotor length of 159 mm within a shell of 179.5 mm length and 86.3 mm inner diameter.

A critical preprocessing step involved creating the negative volume geometry, where the solid rotor components were subtracted from the total mill volume to generate the fluid domain required for CFD meshing. This negative volume creation was essential to avoid interface zone detection errors that would prevent proper simulation setup. A moving mesh approach was implemented to simulate stirrer rotation, with the model

volume divided into inner and outer cell zones using a sliding mesh interface technique to properly capture the complex flow patterns generated by the rotating stirrer.

The mesh generation strategy employed a finite volume method with non-conformal interfaces between rotating and stationary domains. Mesh sizing was optimized to ensure individual particles did not exceed cell dimensions, with minimum mesh size set to 0.0022 m and maximum size to 0.011 m based on the grinding media size range. The k-epsilon turbulence model with standard wall functions was selected to capture the complex flow patterns generated by the high-speed rotating stirrer, with gravity set to -9.81 m/s² in the vertical direction.

Simulation Setup and Parameter Space. The simulation campaign was designed to replicate experimental conditions while extending the parameter space to address computational limitations. Simulations explored tip velocities of 6, 9, and 12 m/s, corresponding to angular velocities ranging from 171.43 to 342.86 rad/s. These velocities maintained consistency with experimental conditions while enabling investigation of velocity scaling effects on grinding performance.

However, computational constraints necessitated the use of larger grinding media sizes ranging from 755 to 2000 µm compared to experimental values of 214 to 800 µm to maintain manageable particle numbers while preserving numerical accuracy. The computational particle count scaling followed established practices, where simulating grinding media sizes down to 214 µm would have resulted in particle numbers exceeding 10^5 under the specified filling conditions, rendering the simulations computationally intractable on available hardware. ΦGM was maintained at 80% to ensure consistent stress conditions and energy transfer efficiency across all simulations, representing typical industrial operation conditions where the grinding chamber volume is optimally utilized while maintaining effective particle circulation.

The Hertz-Mindlin contact model served as the foundation for particle-particle and particle-wall interactions, providing physically realistic representation of collision dynamics through elastic-plastic deformation theory. Material property selection was based on steel grinding media characteristics, with Young's modulus (E) [GPa] set to 200 GPa, Poisson's ratio to 0.3, density to 7850 kg/m³, and restitution coefficient to 0.5 for both particle-particle and particle-wall interactions. Static friction coefficients were set to 0.5 for steel-on-steel contacts, while rolling resistance was configured at 0.1 to account for surface roughness effects and energy dissipation during rolling contacts. Adhesive forces were neglected based on the assumption of clean steel surfaces in aqueous suspension.

Product particles were not explicitly simulated to reduce computational burden, based on the assumption that their kinetic energy was significantly lower than that of grinding media and their motion closely followed fluid flow patterns. This approximation was validated through order-of-magnitude analysis of relative particle velocities

and masses, confirming that product particle dynamics had minimal influence on grinding media motion and stress distributions.

Convergence Criteria and Data Extraction. Simulation convergence was monitored through multiple metrics, with energy dissipation serving as the primary indicator of steady-state achievement. Each simulation was executed for a maximum of 1 second simulation time, equivalent to 27.3-54.6 stirrer rotations depending on angular velocity. This duration proved sufficient to achieve steady-state conditions, typically reached within the first 0.1 seconds as evidenced by stabilization of energy dissipation rates and particle velocity distributions.

The simulation validation and convergence behavior is comprehensively demonstrated in Figure 4, which combines energy distribution analysis, velocity evolution, and fluid flow visualization to validate the CFD-DEM methodology. The energy density distributions show distinct differences between one-way and two-way coupling approaches, with two-way coupling exhibiting higher energy peaks and more efficient energy transfer. The velocity evolution plots demonstrate convergence to steady-state conditions for both coupling methods, while the fluid streamline visualization reveals the complex flow patterns generated by the rotating stirrer geometry.

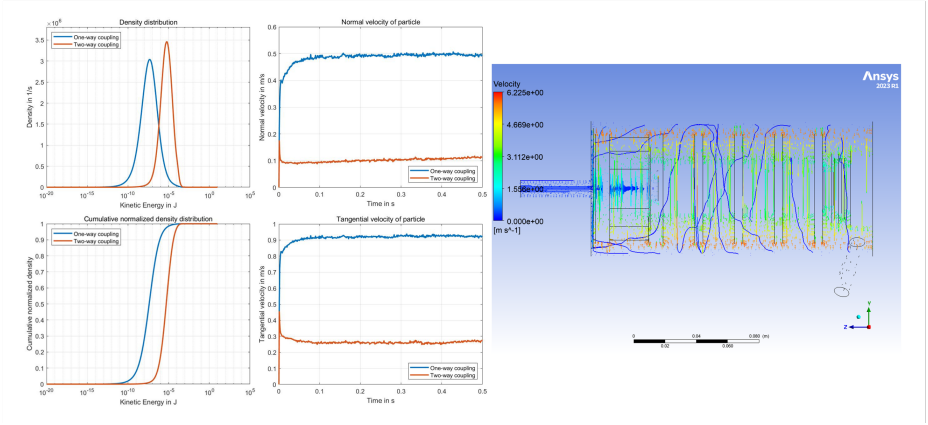

Fig. 4. Comprehensive simulation validation showing (left) energy density distributions and cumulative distributions comparing one-way versus two-way coupling, (center) normal and tangential velocity evolution demonstrating convergence behavior, and (right) fluid streamlines and velocity field visualization illustrating complex flow patterns within the mill geometry

Parameters extracted from the simulations included SE distributions, τ, net M_t on the stirrer, and other dynamic interactions. SE distributions were estimated from collision kinematics. Statistical analysis provided characteristic distribution parameters including 10th, 50th, and 90th percentiles ($SE10$, $SE50$, $SE90$) to characterize the full range

of stress conditions. Net M_t measurements enabled direct comparison with experimental data, while τ distributions provided insights into fluid-phase energy dissipation mechanisms.

2.3 NN-Based Parameter Extrapolation

Motivation and Framework Development. To address computational limitations that prevented direct simulation of experimental grinding media sizes, a Neural Network-Genetic Reinforcement Learning (NN-GRL) framework was employed to align simulation outputs with experimental grinding media sizes. This innovative approach enabled accurate extrapolation of simulation results to match the experimental bead size range by leveraging data generated from simulations with larger beads.

The NN-GRL framework was specifically designed to bridge the parameter gap between simulation capabilities (755-2000 μm) and experimental conditions (214-800 μm), ensuring that the comprehensive insights gained from CFD-DEM simulations could be effectively utilized for analysis of experimental data. This hybrid approach ensured precise prediction of simulation parameters while maintaining consistency with experimental conditions.

Network Architecture and Training Strategy. The NN architecture employed a feed-forward design optimized for distribution prediction tasks, with input variables including v_t and d_{GM}, and output variables comprising key SE distribution characteristics, net M_t, SN, and averaged τ. Rather than predicting complete distribution functions, three characteristic parameters ($SE10$, $SE50$, $SE90$), representing the 10th, 50th, and 90th percentiles of the SE distribution were extracted to reduce computational complexity while preserving essential physical information about the grinding process.

Figure 5 illustrates the complete NN methodology, showing both the complex particle dynamics the network must learn to predict and its architecture for handling the multi-dimensional parameter relationships. The spatial and temporal particle velocity patterns demonstrate the sophisticated physics underlying the grinding process, while the network training progression shows successful convergence to prediction accuracies suitable for engineering applications.

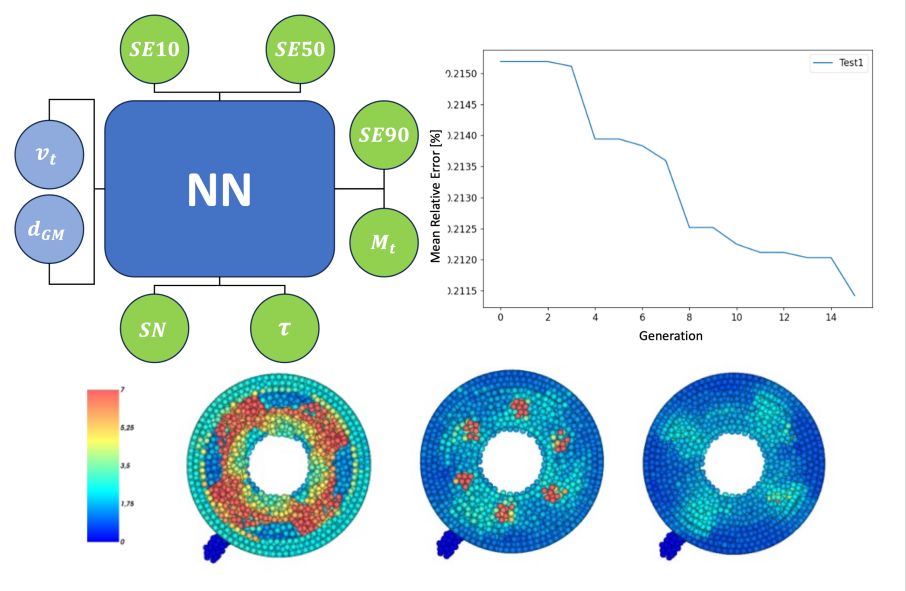

Fig. 5. NN methodology showing (left) network architecture with input parameters (v_t, d_{GM}) and output parameters ($SE10$, $SE50$, $SE90$, M_t, SN, τ), (right) training convergence curve demonstrating error reduction over iterations, and (bottom) spatial-temporal particle velocity patterns illustrating the complex dynamics the network must learn to predict

Data preprocessing included comprehensive normalization procedures where input variables were scaled by their respective orders of magnitude from the baseline simulation (v_t = 6 m/s, d_{GM} = 755 μm) to reduce the span of variable magnitudes from 20 to 3 orders, significantly improving numerical stability and training efficiency. The training database encompassed SE ranges from 10^{-10} to 10^{-4} J, net M_t values from 0.87 to 7.00 Nm, and τ measurements from 13 to 258 Pa after appropriate scaling normalization.

The NN-GRL algorithm combined Reinforcement Learning (RL) with Genetic Algorithm (GA) optimization, executing iterative cycles to minimize prediction errors. Training was conducted over 30 iterations with systematic monitoring of training and validation errors to ensure optimal convergence. The training process demonstrated characteristic rapid initial improvement followed by gradual refinement, with mean relative error stabilizing at approximately 0.2% after convergence. This error level was deemed acceptable for engineering applications and below typical experimental uncertainties.

Extrapolation Performance and Validation. Following training completion, inference was performed to generate results for all required v_t-d_{GM} combinations within the

experimental parameter space. The extrapolation procedure successfully generated predictions for grinding media sizes down to 214 μm, effectively bridging the gap between computational and experimental capabilities.

Model validation employed multiple approaches to ensure prediction accuracy across the full parameter space. Cross-validation procedures demonstrated consistent prediction accuracy across all simulation conditions, while sensitivity analysis confirmed physically realistic behavior and appropriate scaling relationships. The successful extrapolation enabled seamless integration of CFD-DEM insights with experimental observations, providing a comprehensive dataset for subsequent analysis.

2.4 Symbolic Regression Methods

Problem Formulation and Theoretical Framework. The symbolic regression problem is formulated as discovering mathematical expressions $f(x)$ that minimize prediction error on experimental datasets $D = \{(x^{(i)}, y^{(i)})\}_{i=1}^{N}$ where $x^{(i)} \in \mathbb{R}^d$ represents input features and $y^{(i)} \in \mathbb{R}$ denotes target values. This constitutes a mixed discrete-continuous optimization problem requiring simultaneous optimization of expression structure $s \in S$ and numerical parameters $\theta \in \Theta(s)$, where S represents the space of syntactically valid mathematical expressions and $\Theta(s)$ denotes the parameter space for structure s.

The optimization objective combines prediction accuracy with structural parsimony through the energy function:

$$E(s, \theta) = L(f_s(X; \theta), y) \cdot (1 + \lambda |s|) \quad (1)$$

where $L(\cdot,\cdot)$ represents the loss function, $|s|$ denotes expression complexity measured as node count, and $\lambda = 0.002$ controls complexity penalization. Mathematical expressions are encoded as abstract syntax trees where internal nodes represent mathematical operators and leaf nodes contain either input variables or numerical constants.

SA-MC Framework. The SA-MC framework combines simulated annealing for global optimization with Markovian state transitions. While employing SA temperature scheduling, the approach satisfies Markov properties through memoryless state transitions where the next state depends only on the current state and move operators. The methodology employs an MCMC approach where each state represents a unique mathematical expression encoded as a syntax tree.

Transition Probability Design and Move Operators. The transition mechanism implements probabilistic distributions over structural modifications using two strategies. Strategy 1 employs a two-stage selection process that first randomly selects from five weighted options [0.81, 0.61, 0.41, 0.19, 0] with probabilities [0.35, 0.3, 0.2, 0.1, 0.05], where only the two lowest values (occurring 15% of the time) trigger size-preserving

moves. Otherwise, the algorithm modifies tree size, with a 35% probability of expansion and 65% probability of reduction. Strategy 2 favors unary insertion (40%) over other move types (20% each), with one option disabled.

The framework employs five core operators: equal-arity replacement substitutes operations while preserving tree structure; unary and binary insertion expand complexity by introducing single-argument functions (sine, logarithm, square root) or two-argument operations (addition, multiplication, division) above existing nodes; unary removal and subtree pruning reduce complexity by eliminating functions or replacing operations with selected operands, preferentially retaining larger subtrees.

Variable selection within operators uses adaptive probability weighting where unused input variables receive double weight (2p) compared to utilized variables (p), encouraging comprehensive feature exploration while maintaining access to successful variable combinations. The move selection strategy follows configurable probability distributions designed to balance exploration with parsimony principles, as illustrated in Figure 6.

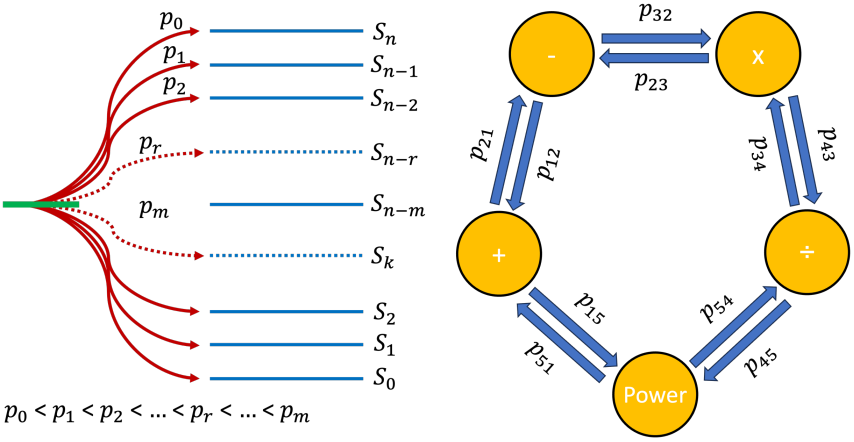

Fig. 6. Energy landscape visualization showing probabilistic state transitions between expression structures S_n through S_0 , with transition probabilities P_0 through P_m illustrating the Metropolis acceptance mechanism and temperature-dependent exploration behavior

SA Integration and Temperature Control. The MCMC exploration integrates with SA through temperature-controlled acceptance probabilities. Given current state s_t with energy $\mathrm{E}(s_t)$, candidate state s' is accepted with probability:

$$P(accept) = min(1, exp(\frac{-\Delta E}{T_t})) \quad (2)$$

where $\Delta\mathrm{E} = \mathrm{E}(\mathrm{s}') - \mathrm{E}(s_t)$ and T_t denotes temperature at iteration t. Initial temperature $\mathrm{T}_{\max}$ is determined through adaptive calibration executing 4,000 trial moves while

iteratively adjusting temperature by factors of 1.5 or 2/3 until achieving target acceptance rate of 0.6. Linear cooling follows $T_t = T_{max} - (T_{max} - T_{min}) \cdot \frac{t}{\text{steps}}$.

Constant Optimization Strategy. Following structural modifications, the framework optionally applies MCMC-based refinement to numerical constants. This secondary optimization employs bounded random walk transitions where the next parameter value is generated as $k_{i+1} = k_i + \varepsilon_i \cdot \delta$, with direction $\varepsilon_i \in \{-1, +1\}$ randomly selected and step size δ adaptively controlled through exponential decay with factor 0.6 following unsuccessful moves. The complete algorithmic workflow is shown in Figure 7.

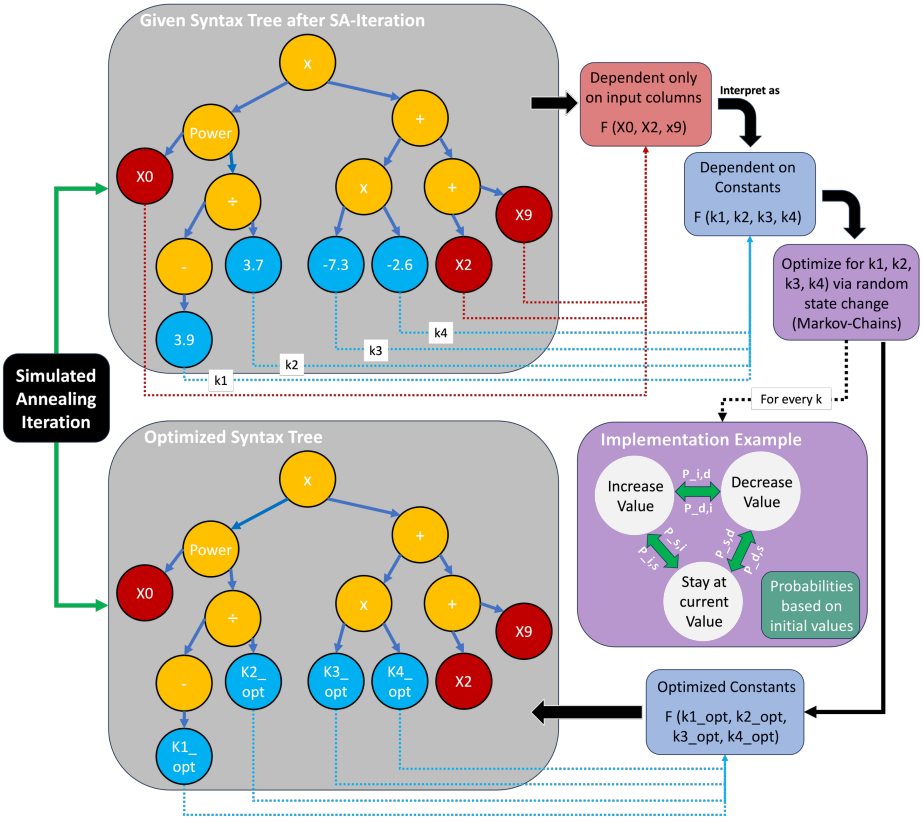

Fig. 7. Complete algorithmic workflow showing the integration of structural MCMC exploration with constant optimization, including initialization procedures, move operator selection, Metropolis acceptance decisions, temperature scheduling, and convergence monitoring mechanisms

Implementation Framework. The framework implements comprehensive protection mechanisms ensuring robust evaluation across diverse input domains. Protected divi-

sion returns unity when denominator magnitude falls below threshold $\varepsilon = 0.01$, preventing singularities while maintaining mathematical interpretability. Protected logarithm operations handle negative arguments through absolute value transformation, returning zero for arguments below 0.001 to avoid numerical instabilities. Protected square root applies absolute value preprocessing, while protected exponentiation bounds exponents to [-4, 4] and operates on absolute bases.

Expression evaluation employs recursive tree traversal with vectorized NumPy operations, achieving computational complexity $O(|s| \cdot N)$ where $|s|$ represents expression size and N denotes dataset size. Overall algorithmic complexity scales as $O(G \cdot |s|_{avg} \cdot N)$ where G represents generations, $|s|_{avg}$ denotes average expression size (typically 10-20 nodes), and N indicates dataset size. Individual operation complexities contribute: expression evaluation $O(|s| \cdot N)$, move generation $O(|s|)$, energy computation $O(N)$, and constant optimization $O(I \cdot N)$ where I represents MCMC iterations (15).

The energy function supports multiple loss functions through modular evaluation architecture. Mean Absolute Percentage Error (MAPE) provides scale-invariant assessment particularly suitable for materials science applications, while the coefficient of determination (R^2) measures explained variance proportion, offering intuitive model quality assessment.

Benchmark Symbolic Regression Frameworks. To evaluate SA-MC performance, we benchmark against five established frameworks representing diverse algorithmic paradigms. PySR combines evolutionary algorithms with gradient-based optimization through multi-population genetic programming, leveraging Julia's SymbolicRegression.jl backend for efficiency while providing Python interface and advanced features such as simulated annealing, automatic complexity control, and dimensional analysis. GPLearn follows standard tree-based genetic programming principles with scikit-learn compatibility, offering simplicity and standardized fit/predict interfaces. PhySO introduces physics-informed symbolic regression by embedding dimensional analysis and physical constraints directly into the search process, combining genetic programming for structural discovery with gradient-based parameter refinement. SyBReN applies physics-inspired, data-driven modeling in applied industrial contexts such as battery electrode processing. Together, these frameworks span evolutionary, physics-informed, and neural-network-driven approaches, enabling comprehensive evaluation across multiple methodological dimensions.

3 Results and Discussion

3.1 CFD-DEM Simulation and NN Extrapolation

The comprehensive CFD-DEM simulation campaign generated a detailed database encompassing nine distinct operating conditions with systematic variation of tip velocity

and grinding media diameter. Eight of the nine planned simulations were successfully completed, with simulation 3 (12 m/s, 755 µm) experiencing convergence issues due to high computational complexity that prevented complete data extraction. The missing values from simulation 3 were subsequently filled through interpolation using the trained NN on the remaining dataset to ensure completeness of the simulation database. The complete simulation trends are illustrated in Figure 8, which summarizes the extracted parameters (M_t, τ, $SE10$, $SE50$) across simulated d_{GM} and v_t.

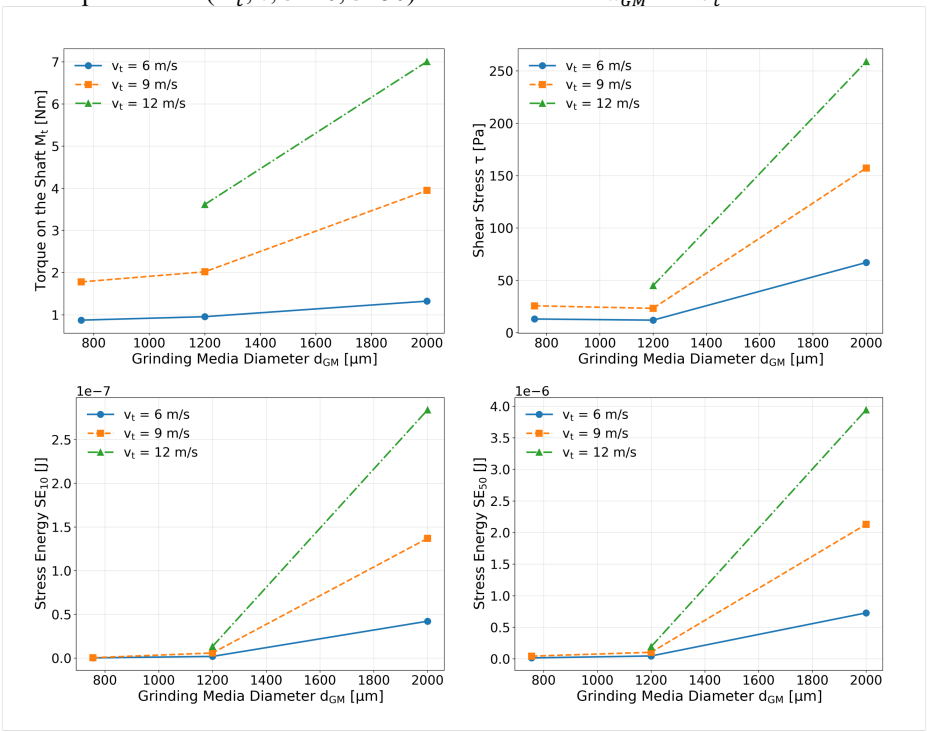

Fig. 8. CFD-DEM simulation results for (top left) M_t , (top right) τ, (bottom left) $SE10$, and (bottom right) $SE50$ as a function of d_{GM}. All quantities increase monotonically with d_{GM} and v_t, though data at v_t=12 are limited to two d_{GM} sizes.

The parameter sensitivity analysis reveals the complex relationships between operating conditions and grinding performance, as demonstrated in Figure 9. The multi-parameter investigation shows systematic scaling of particle velocities with rotational speed, material properties, and grinding media diameter, providing quantitative validation of the physical relationships underlying the grinding process.

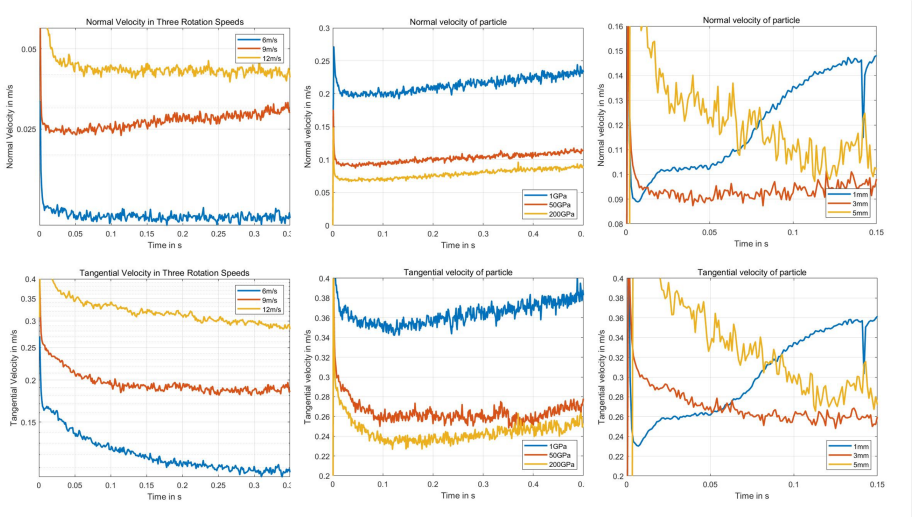

Fig. 9. Multi-parameter sensitivity analysis showing normal and tangential velocity responses to (left column) $v_t$variations (6, 9, 12 m/s), (center column) E variations (1, 50, 200 GPa), and (right column) d_{GM}variations (1, 3, 5 mm), demonstrating the complex parameter relationships the NN must capture for accurate extrapolation

SE distributions exhibited characteristic behavior with distribution parameters showing systematic dependence on operating conditions. Higher v_t resulted in broader distributions with increased mean SE, consistent with enhanced grinding efficiency. The $SE10$, $SE50$, and $SE90$ values demonstrated clear scaling relationships with both v_t and d_{GM}, providing quantitative validation of theoretical grinding models.

Net M_t measurements from simulations ranged from 0.87 to 7.00 Nm across the parameter space, with systematic increases corresponding to higher v_t and larger d_{GM}. These M_t values provided essential validation data for comparison with experimental measurements and served as key inputs for energy efficiency calculations. The M_t scaling followed expected trends, with larger media requiring greater energy input due to increased collision frequencies and intensities.

τ measurements revealed significant variation across operating conditions, ranging from approximately 13 to 258 Pa after appropriate scaling. The systematic variation of τ with operating parameters provided insights into fluid-phase energy dissipation mechanisms and their contribution to overall grinding efficiency. Higher τ correlated with increased v_t and enhanced fluid turbulence in high-energy grinding conditions.

NN Extrapolation Results. The trained NN successfully extrapolated simulation results to experimental grinding media sizes, generating comprehensive predictions for all experimental conditions. The extrapolation process produced a complete dataset covering the experimental parameter space, with d_{GM} ranging from 214 to 800 µm and

v_t spanning 6 to 12 m/s. Notably, the NN was trained exclusively on the eight complete CFD-DEM simulations, with the interpolated data from simulation 3 excluded from the training process to maintain data integrity. Figure 10 shows the NN-augmented results, which reproduce the CFD-DEM values at simulated bead sizes and extend predictions to the experimental range. Unlike the monotonic CFD curves, the augmented results reveal non-linear U-shaped behavior with distinct minima, consistent with the existence of efficiency optima.

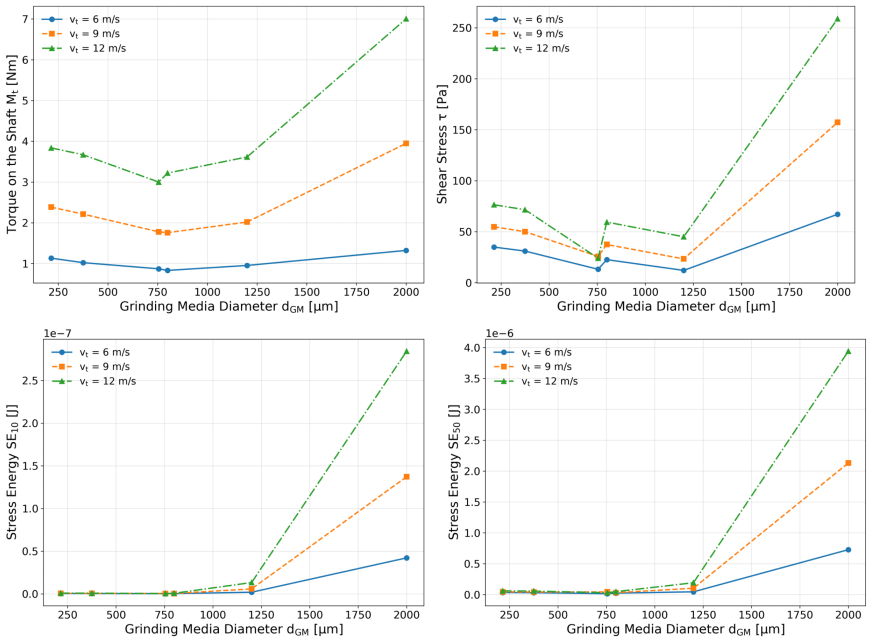

Fig. 10. NN–augmented results for (top left) M_t , (top right) τ, (bottom left) SE 10, and (bottom right) $SE50$. The NN reproduces CFD-DEM results at simulated d_{GM} (755,1200,2000) and extends predictions to experimental used d_{GM} (214,375,800). The augmented curves reveal non-linear U-shaped behavior with minima at intermediate d_{GM}, highlighting the existence of an optimal grinding media diameter.

Comparison between extrapolated and experimental results showed agreement for directly measurable quantities. The extrapolated M_t values demonstrated physically reasonable scaling with d_{GM} and v_t , with predicted decreases in specific M_t as media size increased. This scaling behavior reflected the transition from energy-intensive fine grinding to more efficient coarse grinding regimes.

SE distribution parameters exhibited expected trends, with smaller media sizes generally producing lower individual stress energies but higher stress frequencies. The $SE50$ values for experimental conditions ranged from approximately 2.3×10^{-8} to

6.0×10^{-8} J, representing typical stress energies for fine grinding applications. The systematic scaling of SE with d_{GM} provided quantitative validation of fundamental grinding theory.

Integrated Dataset Validation and Quality Assessment. The combined experimental and simulation datasets provided comprehensive coverage of the grinding parameter space, with experimental data capturing real-world process behavior and simulation data extending insights into stress distributions and flow field characteristics not accessible through experimental measurements alone. The NN extrapolation successfully bridged the parameter gap between simulation and experimental conditions, enabling seamless integration of both data sources.

Cross-validation between experimental and computational results demonstrated satisfactory agreement for overlapping parameter ranges, confirming the reliability of both methodologies. The integration of experimental measurements with CFD-DEM simulation data provided unprecedented insight into grinding physics, combining the accuracy of experimental observations with the detailed process understanding enabled by computational analysis.

The NN extrapolation methodology proved highly effective in bridging computational and experimental scales, with prediction accuracies well within engineering tolerances. The comprehensive validation procedures ensured that the integrated dataset accurately represented grinding physics across the full parameter space, providing a robust foundation for subsequent symbolic regression analysis and physics-based model development.

The resulting integrated dataset encompassed process configuration input parameters, measured parameters and simulation-based calculated parameters. This comprehensive framework provided the necessary data richness to capture the complex physics governing wet ball grinding processes, and serves as the foundation for subsequent symbolic regression analysis aimed at deriving physics-based models for critical grinding parameters. The comprehensive parameter coverage and high-fidelity data generation methodology ensure robust model discovery capabilities for advancing the fundamental understanding of wet ball grinding physics and particle size reduction mechanisms.

3.2 Symbolic Regression Methods Benchmark Performance Analysis

The evaluation of symbolic regression frameworks reveals that optimal performance depends critically on problem characteristics rather than universal algorithmic superiority. This investigation examines six frameworks—SA-MC, PySR, PhySO, SyBReN, gplearn, and SA—across benchmark equations and experimental grinding data to demonstrate that successful process optimization requires strategic method selection and ensemble approaches.

Benchmark Performance Analysis. The evaluation across ten benchmark equations reveals significant performance variations dependent on equation complexity and structural characteristics. The results demonstrate that optimal framework selection is inherently problem-dependent and benefits from ensemble approaches rather than single-method solutions.

The complete benchmark suite in Table 1 and Table 2 ranges from simple proportionalities to complex nested expressions, with equations numbered 1-10 from top to bottom in order of increasing complexity. For simple equations (Eq.1-Eq.3), all frameworks achieved near-perfect performance with R^2 values exceeding 0.99, confirming baseline competence across methodologies. However, performance divergence becomes pronounced as complexity increases, with each framework exhibiting distinct strengths and limitations. The benchmark suite was constructed using synthetic datasets, with approximately 200 data points generated per equation.

Table 1. Benchmark equations with comparative SA and SA-MC performance results showing execution times and R^2 accuracy values across increasing mathematical complexity from simple proportionalities to nested expressions with dimensionless groups

Equations	t_SA	R^2_SA	t_SA-MC	R^2_SA-MC
$\mathrm{Y_s} = 0.5 \cdot \hat{\mathrm{Y}}_\mathrm{f}$	1.6	1	17	1
$\mathrm{SI} = 2.5 \cdot \gamma \cdot \eta$	18.5	1	14	0.99999
$\mathrm{N} = \frac{\gamma \cdot t_D}{4\pi}$	15.7	1	20	0.96
$\mathrm{k_x} = 0.98 + 0.02 \cdot (\frac{c_x}{c_c})^{2.25}$	74.7	0.634	18	0.74
$\dot{\mathrm{V}}_\mathrm{k} = \frac{1}{2} \cdot \pi \cdot d_{fa} \cdot \mathrm{n} \cdot d_f \cdot I_s \cdot \mathrm{z} \cdot z_w$	38.76	1	47.35	0.99999
$\mathrm{SE} = \left(\frac{1}{3}\right) \cdot x^3 \cdot \pi^2 \cdot \hat{\eta}$	25.7	1	50	0.92265
$\mathrm{x(t)} = x_0 + (x_{end} - x_0) \cdot \frac{t}{(\mathrm{t} + \mathrm{t_k})}$	33.5	0.918	35	0.99996
$\mathrm{SME} = \frac{(\sqrt{3} \cdot \mathrm{V} \cdot (\mathrm{I} - \mathrm{I}^0) \cdot \cos\varphi)}{\dot{\mathrm{m}}}$	113.1	0.619	129.1	0.71
$\mathrm{d_{p}}x = \frac{\mathrm{A}^2\left(1 - \frac{\dot{\mathrm{V}}^*}{A_1}\right)}{\left(1 + \left(\frac{\mathrm{A_3} \cdot \mathrm{n} \cdot \gamma_{\mathrm{crit}}}{\dot{\mathrm{V}}^*}\right)\right)^{0.5}} \cdot \left[1 - \frac{\dot{\mathrm{V}}^*}{A_1}\right]^{-0.5}$	96.2	0.303	22.73	0.9245
$t_E = \frac{18 \cdot \eta \cdot \mathrm{k} \cdot \ln(\frac{\mathrm{r_1}}{\mathrm{r_0}})}{(\rho_{\mathrm{pp}} - \rho_F) \cdot \mathrm{d_p^2} \cdot \omega^2}$	113.1	0.0006	30.47	0.00707

Table 2. Comprehensive comparative performance of six symbolic regression frameworks (gplearn, SyBReN, PySR, PhySO) across ten benchmark equations, showing execution times and R^2 accuracy values for systematic algorithmic capability assessment. This table reports the performance of the remaining methods, complementing the results presented in Table 1.

t_gplearn	R^2_gplearn	t_SyBReN	R^2_SyBReN	t_PySR	R^2_PySR	t_phySO	R^2_phySO
0.3	1	0.02	1	9.86	1	44	1
0.85	0.99993	0.0561	1	10.07	1	46	1
1.29	0.99997	5.89	1	9.93	1	30	1
0.95	0.99069	36.7	0.982	10.23	0.99993	249	0.99026
2.97	0.99862	75.8	1	10.06	1	158	1
1.08	0.99211	0.064	1	10.91	1	55	1
0.85	0.94669	160.2	0.955	9.82	1	453	0.63686
0.87	0.87557	286.9	0.739	10	1	108	0.80592
0.73	0.75964	345.97	0.952	10.06	0.98283	252	0.73137
0.74	0.0745	330.7	0.71	32.72	0.99888	747	0.93313

The evaluation demonstrates complementary strengths across frameworks for process model discovery from empirical data. PySR achieved exceptional performance, reaching $R^2 > 0.99$ for seven equations through multi-population evolutionary optimization with Julia backend, making it optimal when maximum accuracy is prioritized.

PhySO maintained physical consistency with $R^2 > 0.90$ for dimensionally structured equations, providing invaluable theoretical validity for well-understood systems. SyBReN displayed impressive computational efficiency with $R^2 > 0.95$ for the first six equations and rapid execution, ideal for real-time applications.

SA-MC, as an algorithmic approach still in the early stages of development and currently lacking deep learning components (unlike PhySO and SyBReN), demonstrated consistent moderate performance across different complexity levels without exhibiting complete failures. Under certain testing conditions, it even outperformed gplearn, highlighting its potential for exploratory process modeling with experimentally accessible parameters. As shown in Table 1, the comparison also includes the classic SA algorithm, providing a direct baseline. Notably, SA-MC delivered substantial improvements over SA in challenging cases—for example, Eq. 9 improved from $R^2 = 0.303$ to $R^2 = 0.9245$, and Eq. 10 from $R^2 = 0.0006$ to $R^2 = 0.00707$.

gplearn, while showing accuracy degradation for complex expressions ($R^2 < 0.70$ for challenging equations), provides computational efficiency and scikit-learn integration advantages for rapid prototyping and educational applications.

The benchmark results visualized in Figure 11 reveal distinct performance patterns informing framework selection strategies. Simple equations are solved almost instantly by all methods, while complex cases introduce significant variability, with some systems requiring orders of magnitude more computation.

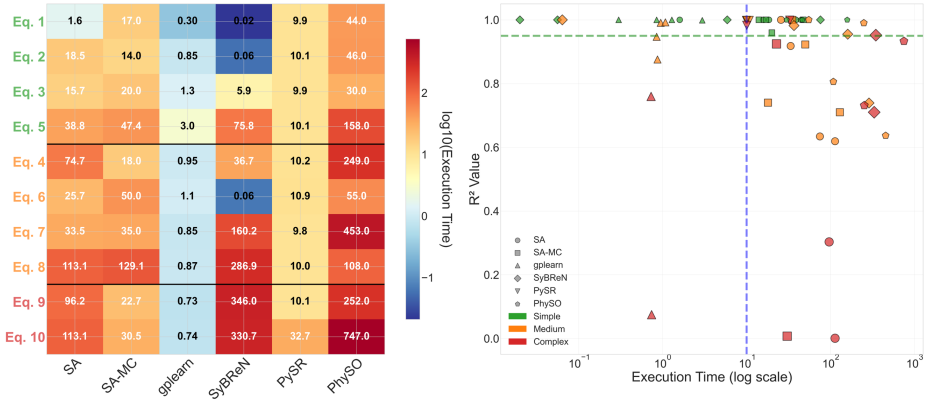

Fig. 11. Performance analysis across mathematical complexity levels showing execution time heatmap with color-coding and accuracy-efficiency scatter plot with performance threshold reference lines

SA-MC reliably appeared near the optimal region, reaching accuracy levels above $R^2 > 0.95$ for multiple equations while keeping computation times competitive. The method shows particular promise as a robust screening tool for initial model discovery before applying specialized methods for refinement. SA-MC's performance on benchmark equations illustrates current capabilities and development opportunities. For the kinetic size evolution equation x(t) (Eq.7), the method captured the overall functional form with some deviation in transition regions. The particle size correlation d_{px} (Eq.9) presented greater challenges, with SA-MC recovering the general relationship structure but showing variability in fine-scale fitting as shown in Figure 12, reflecting areas for algorithmic refinement in handling complex nested expressions.

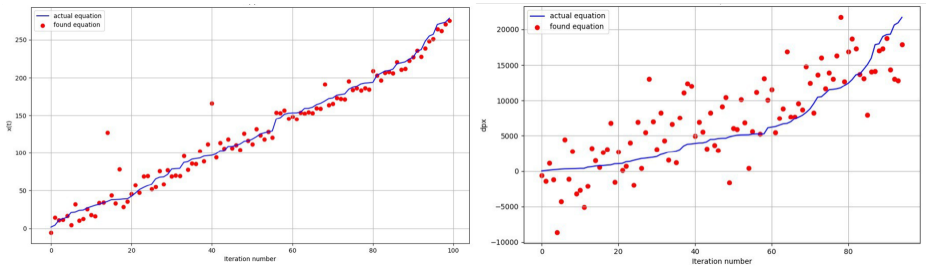

Fig. 12. SA-MC equation recovery for benchmark equations: Eq. 7 (x(t), left) and Eq. 9 (d_{px}, right).

Process Engineering Applications. Application to experimental grinding data reveals how framework selection impacts solution quality and practical utility. Each method discovered different mathematical relationships, reflecting distinct algorithmic approaches and optimization strategies.

Table 3. E_m prediction results showing discovered mathematical expressions with R^2 accuracy values and MAPE error metrics, demonstrating trade-offs between prediction accuracy and parameter accessibility for process control applications

Method	Equations	R^2	MAPE
PySR	$E_m = \frac{0.86382 \cdot t_Z \cdot [t_Z + (d_{GM} \cdot n^3 + v_t)^3]}{m_p}$	0.9943	0.2907
SyBReN	$E_m = \frac{0.94 \cdot t_Z \cdot (4.25 \cdot 10^{12} \cdot d_{GM}^2 - 1.79 \cdot 10^5) + 2.2 \cdot 10^4 \cdot m_p}{m_p}$	0.9809	0.7870
PhySO	$E_m = -104694.23271 \cdot d_{GM}^2 \cdot n^3 \cdot (c_v \cdot t_Z - t_Z)$	0.9027	0.9050
PySR	$E_m = 3999.0002 \cdot \left(\frac{SN \cdot d_{GM}^3 \cdot v_t^2}{m_p}\right)$	0.9999	$5 \cdot 10^{-8}$
SyBReN	$E_m = 1003.2136 \cdot \left(\frac{\rho_{GM} \cdot SN \cdot d_{GM}^3 \cdot v_t^2}{m_p}\right)$	0.9999	0.0009
PhySO	$E_m = 93705.7462827001 \cdot t_Z \cdot d_{GM}^2 \cdot n^3 - v_t^2$	0.8915	0.8455
SA-MC	$E_m = v_t^2 \cdot t_z^{v_t^{d_{GM} \cdot \frac{n}{2}} \cdot c_v^{-5.783 \cdot d_{GM} \cdot n}}$	0.8808	26.228
PySR	$E_m = \frac{n \cdot t_Z \cdot v_t^3 + t_Z^2}{m_p + n}$	0.9664	0.1505
PhySO	$E_m = 0.13284 \cdot n \cdot t_Z \cdot v_t^2 \cdot (0.38737 - c_v)$	0.9274	0.2867
SyBReN	$E_m = 0.000266 \cdot SN \cdot d_{GM}^2 \cdot v_t^3$	0.7527	0.2531

The Em equation results reflect three distinct dataset configurations that reveal the frameworks' ability to reconstruct theoretical relationships from different parameter combinations. The first three equations were generated using datasets without SN and SE parameters, where Em values came from simulation. Remarkably, frameworks were able to discover relationships incorporating the underlying physics that SN and SE represent—stress-related parameters (like circumferential velocity, media diameter, and

rotational frequency) and energy-related quantities—even without explicit access to these derived variables.

The following four equations used datasets including SN and SE as input parameters, with Em also from simulation. These results demonstrate how frameworks leverage pre-calculated theoretical quantities to achieve exceptional accuracy, with PySR and SyBReN reaching R^2 values of 0.99999.

The final three equations represent the most practically relevant scenario: SN and SE from simulations as inputs, but Em measured experimentally. This configuration tests the frameworks' ability to predict real measured quantities using simulation-derived theoretical parameters, achieving R^2 values ranging from 0.75 to 0.93.

SA-MC discovered relationships using experimentally accessible parameters, achieving $R^2 = 0.8808$ with MAPE = 26.2289 for specific energy prediction. The framework demonstrated ability to identify stress-energy relationships through experimental parameters, incorporating blocks containing m_{GM}, velocity-related terms, and geometric factors that align with stress number theory.

Different frameworks discovered exponential, rational, and polynomial relationships, suggesting multiple valid mathematical representations of the underlying physical process. High-accuracy solutions consistently required simulation-derived parameters, while experimental-only approaches achieved moderate accuracy through complex nonlinear combinations of controllable variables.

Notably, several discovered expressions show remarkable correspondence with established theoretical models. The Kwade energy model (3) [13] provides the theoretical foundation for specific energy in grinding:

$$E_m = \frac{SN \cdot SE}{m_p} = \frac{\frac{\varphi_{GB}\,(1-\varepsilon)}{(1-\varphi_{GB}\cdot(1-\varepsilon))\cdot c_v}\cdot\left|\frac{n\cdot t_Z}{d_{GM}}\right|\cdot d_{GM}^3\cdot\rho_{GM}\cdot v_t^2}{m_p} \tag{3}$$

In this Kwade energy model, the SN is represented by the fraction preceding the multiplication with the SE; its leading block contains φ_{GB} , ε, and c_v, and is typically constant for a given process configuration. The SE is given by the second block, which includes d_{GM} , ρ_{GM} , and v_t. This separation illustrates how several of the tested symbolic regression frameworks capture both the process-dependent frequency of SN and the energy transferred per event SE.

Most of SyBReN's E_m found models incorporate a block containing ρ_{GM} , SN, d_{GM} , v_t, and that corresponds directly to key components of the Kwade theoretical framework shown above. This structural alignment validates that the frameworks can recover physically meaningful relationships, even when not explicitly constrained by theoretical models.

Table 4. SN prediction results showing discovered mathematical expressions with R^2 accuracy values and MAPE error metrics for different symbolic regression frameworks

Method	Equations	R^2	MAPE
PySR	$SN = \frac{0.07628 \cdot t_Z \cdot (n + 2.08341)}{(d_{GM} + 0.00401)^4}$	0.9943	0.0446
SyBReN	$SN = 194718740 \cdot n \cdot t_Z + 2.7 \cdot \frac{t_Z \cdot n}{d_{GM}^2}$	0.9809	0.1064
SA-MC	$SN = t_Z \cdot (11 \cdot n)^{5.47}$	0.9630	0.1680
PhySO	$SN = t_Z \cdot n \cdot (271126041.89809 - 542252085.79618 \cdot c_v)$	0.9543	0.1641
SyBReN	$SN = \frac{12.9 \cdot t_Z \cdot n}{d_{GM}^2}$	0.7790	0.5021
gplearn	$SN = \frac{t_Z^2 \cdot n\,(n - 0.804)}{d_{GM}}$	0.6204	0.7072

The diversity of discovered expressions for stress number prediction illustrates the data-dependent nature of symbolic regression outcomes. PySR achieved near-perfect accuracy ($R^2 = 0.9943$, MAPE = 0.2907) using accessible process parameters, demonstrating the method's ability to reconstruct the relationships underlying SN through combinations of fundamental variables like d_{GM}, v_t, and operational parameters.

SyBReN generated comparable accuracy ($R^2 = 0.9809$) for stress number prediction, showing consistent performance while maintaining computational efficiency. The discovered stress number expressions consistently featured parameter combinations involving d_{GM}, v_t, and rotational parameters, effectively reconstructing the theoretical basis of stress number calculations through empirical discovery.

PhySO produced physically consistent expressions but with reduced accuracy ($R^2 = 0.9027$), illustrating the trade-off between dimensional correctness and empirical fitting in complex systems.

SA-MC discovered stress number relationships using experimentally accessible parameters, incorporating blocks containing media-related terms and velocity factors that align with stress number theory, though achieving moderate accuracy levels as expected for a developing framework.

Table 5. Comprehensive x_{50} prediction results showing diverse mathematical expressions with accuracy metrics, highlighting universal challenges in particle size evolution modeling and identification of physically meaningful scaling relationships

Method	Equations	R^2	MAPE
PySR	$x_{50} = \frac{55537.81899}{(M_t - 0.47214)(t_Z + \frac{\mathrm{V}}{M_t - 0.54823})}$	0.9403	0.3698
PySR	$x_{50} = \frac{377.46445 \cdot m_{GM}}{(E_m + 16863.617)(-SE \cdot n + c_v)} - 1.048178$	0.9208	0.6506
PhySO	$x_{50} = -SE + T - \frac{826327.22129}{-M_t \cdot t_Z \cdot v_t - 590.37347}$	0.9183	0.7215
PySR	$x_{50} = \frac{911.82623 \cdot m_P}{{M_t}^2 \cdot t_Z + 194.8095}$	0.9027	0.5229
PhySO	$x_{50} = \frac{77516.55773 \cdot n}{(M_t \cdot v_t \cdot t_Z + 14.28966 \cdot n + n) \cdot \ln(n)}$	0.8820	0.5540
SyBReN	$x_{50} = \frac{100852.44}{M_t \cdot t_Z + 2n}$	0.8692	0.6309
SyBReN	$x_{50} = \frac{66213.95}{M_t \cdot t_Z + \mathrm{V}}$	0.8348	0.3785
PhySO	$x_{50} = \left(T - \frac{c_v - 224310815.84904}{M_t \cdot t_Z \cdot v\mathrm{t}}\right)^{0.5}$	0.8274	1.5749
SyBReN	$x_{50} = \frac{3453.73 \cdot m_{GM}}{E_m + m_{GM} \cdot (-SE \cdot (E_m - m_p \cdot t_z) + 1.877)}$	0.8198	0.4593

Median particle size prediction presented the greatest challenge across all frameworks. Multiple particle size percentiles were evaluated (x_{10}, x_{50}, x_{90}), with x_{50} delivering the best results across methods, though even these optimal results remained challenging. The best-performing methods struggled, with PySR reaching $R^2 = 0.94$ at best, indicating fundamental limitations of purely empirical approaches for complex multi-physics grinding processes.

SA-MC achieved relatively low numerical accuracy but demonstrated capability in identifying the scaling relationship (4) This relationship captures essential physical dependencies and relatively aligns with established grinding theory expectations. While quantitative performance requires development, SA-MC's ability to extract physically meaningful parameter combinations represents capability for process understanding:

$$x_{50} \propto \mathrm{T} \cdot m_{GM} \cdot \frac{V}{t_Z \cdot n} \tag{4}$$

Dimensional Consistency. Symbolic regression does not inherently enforce dimensional consistency unless explicit constraints are applied. Several identified equations achieve excellent predictive accuracy but lack balanced units between equation sides.

Large numerical constants (e.g., 3999.0002, 93705.746) effectively absorb hidden unit conversions, resulting in strong empirical fits but limited physical interpretability.

Examples include the fourth E_m equation yielding near-perfect fits while relying on constants to compensate for dimensional mismatch, and the second x_{50} equation predicting trends accurately despite mixing incompatible dimensions. Conversely, the fifth, sixth, and eighth E_m equations maintained full dimensional consistency with correct [m²/s²] units.

While frameworks like SyBReN and PhySO enable dimensionality analysis and unit constraint enforcement, their application substantially reduced predictive performance, likely due to the small dataset, modeling difficulty for E_m, SN, and x_{50}, and wet ball grinding's multiphysics complexity.

Framework Selection and Optimization Strategy. In Figure 13 the correlation analysis revealed complex interdependencies between process parameters and grinding performance metrics. Strong negative correlations emerged between circumferential velocity and median particle size, confirming expected energy input relationships.

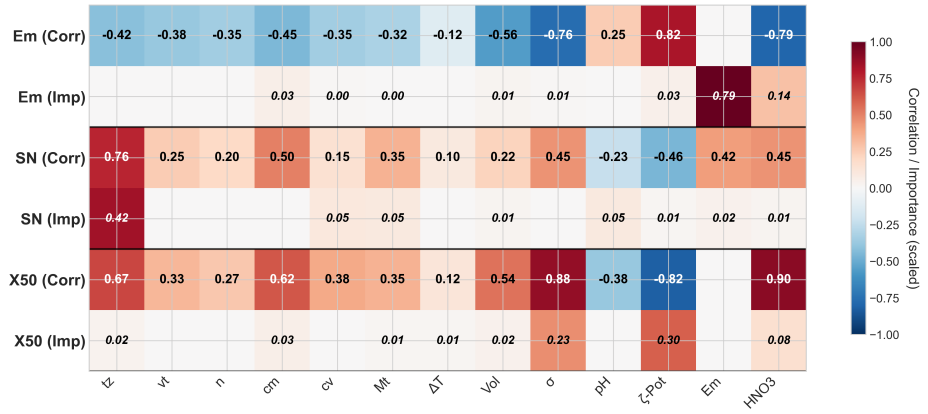

Fig. 13. Correlation matrix and feature importance analysis showing Pearson correlation coefficients between grinding performance metrics (E_m, SN , x_{50}) and operational variables including circumferential velocity, media properties, and process conditions

Feature importance analysis identified circumferential velocity as the dominant factor across metrics, with media diameter showing secondary importance for stress-related parameters. These patterns validate physical relationships captured in symbolic regression expressions despite numerical accuracy limitations.

The comprehensive evaluation demonstrates that optimal performance requires strategic framework selection based on problem characteristics. When maximum accuracy is paramount with simulation-derived parameters available, PySR provides superior

performance with computational costs justified by exceptional quality. For dimensional consistency and physical interpretability, PhySO offers optimal accuracy-theoretical soundness balance. When rapid execution is critical, SyBReN provides competitive accuracy with efficient inference. When experimental parameters are prioritized, SA-MC demonstrates consistent performance avoiding complete failure while providing interpretable results.

Optimal symbolic regression performance requires ensemble strategies rather than single-method approaches. Each framework excels in different scenarios—PySR for accuracy, PhySO for physics consistency, SyBReN for efficiency, SA-MC for robustness. Combining strengths addresses individual limitations.

Running multiple frameworks provides confidence assessment and reveals alternative mathematical representations. Hybrid approaches can utilize high-accuracy simulation-based expressions for design optimization while maintaining interpretable experimental-parameter relationships for process control.

Framework selection impacts both model accuracy and practical implementation feasibility. High-accuracy expressions require simulation support, creating computational bottlenecks in real-time optimization. Experimental-parameter expressions enable direct process control with reduced precision. Successful optimization balances accuracy with implementation constraints, often favoring moderately accurate, directly implementable relationships over highly accurate but computationally demanding alternatives.

These findings highlight a central trade-off: unconstrained symbolic regression effectively generates accurate empirical surrogates at the cost of physical interpretability, while dimensionally constrained approaches preserve validity but may underperform in data-limited, process-complex scenarios. Future work could address this through dimensionless π-groups (Buckingham's π-theorem) or refined constraint strategies balancing accuracy with interpretability.

Correlation Analysis versus Symbolic Regression. The correlation analysis reveals important disconnects: not all parameters in discovered equations score highly in correlation analysis. This commonly occurs when comparing symbolic regression with correlation or feature importance scores, reflecting fundamental approach differences.

Correlation analysis captures linear pairwise relationships, while symbolic regression discovers nonlinear multivariate interactions. Variables may show weak individual correlation but become critical when combined through multiplication, division, or exponential operations. For E_m equations, terms like v_t^2 or d_{GM}^3 may not correlate strongly individually, but their interaction with SN, ρ_{GM}, and m_{GM} creates predictive power.

Feature importance metrics are typically normalized or model-specific, while symbolic regression may exploit parameters with small raw influence but large structural

importance. The framework balances fit quality with simplicity, sometimes retaining variables appearing unimportant by correlation because they improve structural generalizability through dimensional balancing or scaling effects.

Multicollinearity complicates this relationship. Correlated inputs like σ, PH , and ζ may have importance distributed across multiple correlation coefficients, while symbolic regression selects specific combinations. This fundamental difference means correlation identifies features tracking output linearly, while symbolic regression determines which feature combinations explain output through complex interactions.

The results demonstrate that advancing symbolic regression for process engineering requires moving beyond single-method approaches toward integrated frameworks leveraging complementary algorithmic strengths. Rather than seeking the "best" method, focus should shift to optimal combination strategies adapting to specific problem characteristics and application requirements. This data-dependent optimization acknowledges that symbolic regression success depends critically on alignment between algorithmic capabilities and problem structure, suggesting future developments should emphasize ensemble methods and adaptive framework selection rather than universal algorithmic improvements.

Model Generalizability and Limitations. The generated Em, SN, and x_{50}models achieve high accuracy on the experimental dataset but do not guarantee generalizability to other milling systems, materials, or configurations. The absence of d_{GM} from discovered x_{50} equations, despite extensive literature demonstrating its critical role in particle size evolution, exemplifies this limitation. While equations describe the current dataset effectively and could enable process automation in identical industrial settings, they would likely deliver inaccurate results for different systems.

However, models contain generalizable components aligning with established theory. SN equations feature tn and d_{GM} blocks, while the SyBReN E_m equation incorporates blocks with ρ_{GM}, SN, d_{GM}, v_t, and m_P corresponding directly to the Kwade energy model, validating physical relevance beyond specific experimental conditions.

4 Conclusion and Outllok

This study demonstrates the successful integration of experimental grinding data with CFD-DEM simulations through NN extrapolation and symbolic regression frameworks, establishing a comprehensive methodology for discovering interpretable mathematical models in wet ball grinding processes. The hybrid approach combining laboratory experiments with computational simulations enabled extraction of process parameters previously inaccessible through experimental measurements alone, particularly stress energy distributions and shear stress fields that govern particle breakage mechanisms.

The systematic benchmarking of six symbolic regression frameworks revealed that optimal model discovery requires strategic method selection based on specific application requirements rather than universal algorithmic superiority. PySR demonstrated exceptional accuracy when simulation-derived parameters were available, achieving R^2 values exceeding 0.999 for energy models incorporating stress number and stress energy terms. PhySO maintained dimensional consistency crucial for theoretical validity, while SyBReN provided computational efficiency essential for real-time applications. The in this work developed SA-MC framework, despite moderate numerical accuracy, successfully identified physically meaningful parameter relationships using experimentally accessible variables, demonstrating potential for industrial deployment where simulation support remains impractical.

Discovered mathematical expressions exhibited remarkable alignment with established theoretical frameworks, particularly the Kwade energy model. Multiple frameworks independently recovered parameter blocks containing ρ_{GM}, SN, d_{GM}, v_t, and m_P that correspond directly to theoretical stress-energy relationships, validating that data-driven approaches can reconstruct fundamental physics without explicit theoretical constraints. However, the absence of d_{GM} from particle size evolution models and dimensional inconsistencies in some high-accuracy expressions highlight the inherent tension between empirical accuracy and physical interpretability.

The primary limitation concerns model generalizability beyond the specific experimental configuration. While discovered expressions achieve high accuracy on training data and contain theoretically meaningful components, their applicability to different mill geometries, materials, or operating conditions remains unvalidated. The small dataset size and focus on aluminum oxide processing restricts the scope of conclusions. Additionally, particle size prediction proved challenging across all frameworks, with best-performing methods achieving R^2 values below 0.95, indicating fundamental limitations in purely empirical approaches for complex multiphysics processes.

Looking forward, this research establishes the foundation for advanced process monitoring and control systems in industrial grinding operations. Future development will focus on integrating discovered particle size evolution models into a Digital Twin framework with real-time mill communication capabilities. As illustrated in Figure 14, this system enables dynamic forecasting of grinding progression, predicting time-to-target particle size through continuous model updating based on live sensor data. The Digital Twin architecture incorporates torque measurements, conductivity monitoring, and periodic particle size verification to refine predictions throughout operation, transforming static empirical models into adaptive process optimization tools.

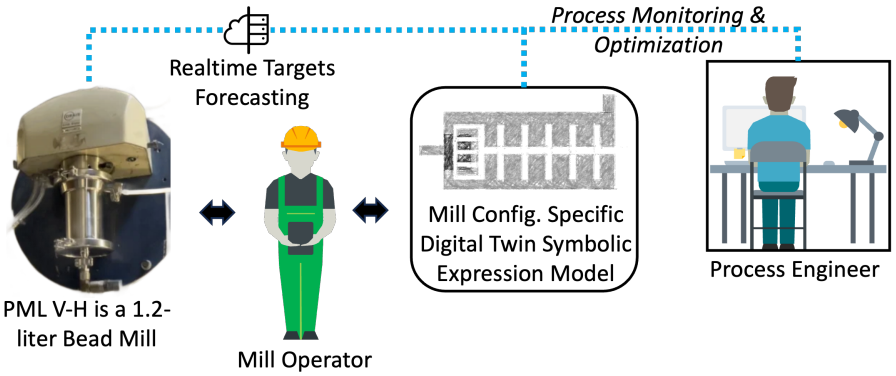

Fig. 14. Digital Twin framework for real-time particle size evolution forecasting in wet ball grinding, showing integration of symbolic regression models with live mill sensor data, automated particle size analysis, and predictive control optimization for achieving target specifications.

Future work will also address several critical areas to advance symbolic regression applications in process engineering. Expanding experimental datasets across diverse materials and mill configurations would enhance model generalizability and reveal universal scaling relationships. Incorporating dimensionless groups through Buckingham π-theorem could balance empirical accuracy with theoretical consistency. Development of ensemble methods combining multiple symbolic regression frameworks could leverage complementary strengths while mitigating individual limitations. Integration with reinforcement learning algorithms would enable autonomous process optimization, adjusting operating parameters in real-time based on evolving model predictions.

The transition from laboratory-scale model development to industrial implementation requires addressing computational efficiency, sensor reliability, and model uncertainty quantification. Successful deployment demands robust frameworks handling noisy industrial data, partial sensor failures, and process disturbances while maintaining prediction accuracy. The Digital Twin concept represents a paradigm shift from reactive process control to predictive optimization, potentially reducing energy consumption, improving product quality, and minimizing operational costs across comminution operations.

This work demonstrates that symbolic regression can bridge the gap between black-box machine learning and mechanistic modeling in process engineering, providing interpretable models that maintain physical relevance while achieving competitive predictive performance. The successful reconstruction of theoretical relationships from empirical data validates the approach's potential for discovering novel process understanding and enabling next-generation industrial automation systems.

Code Availability: The SA-MC symbolic regression framework developed in this study is available as open-source software at [https://github.com/ah-medeisa2]. Benchmark equations and evaluation scripts are included in the repository.

References

1. Rittinger, P.R.: *Lehrbuch der Aufbereitungskunde*. Ernst & Korn (1867).
2. Kick, F.: *Das Gesetz der proportionalen Widerstände*. Leipzig (1885).
3. Bond, F.C.: The third theory of comminution. *Trans. AIME* 193, 484–494 (1952).
4. Hukki, R.T.: Proposal for a solomonic settlement between the theories of Rittinger, Kick and Bond. *Trans. AIME* 220, 403–408 (1961).
5. Meloy, T.P.: Dimensional analysis for size reduction. *Powder Technology* 7(2), 109–112 (1973).
6. Austin, L.G., Klimpel, R.R., Luckie, P.T.: *The Process Engineering of Size Reduction: Ball Milling*. SME, New York (1984).
7. Herbst, J.A., Fuerstenau, D.W.: Fundamentally based load control strategy for tumbling mills. *Powder Technology* 75(1), 21–28 (1993).
8. Napier-Munn, T.J., Morrell, S., Morrison, R.D., Kojovic, T.: *Mineral Comminution Circuits: Their Operation and Optimization*. JKMRC, Brisbane (1996).
9. King, R.P.: *Modeling and Simulation of Mineral Processing Systems*. Butterworth-Heinemann, Oxford (2001).
10. Hinde, A.L., et al.: Population balance modeling of milling. *Minerals Engineering* 17(11–12), 1193–1200 (2004).
11. Austin, L.G., Bagga, P.: An analysis of fine dry grinding in ball mills. *Powder Technology* 28(1), 83–90 (1981).
12. Kwade, A.: Wet comminution in stirred media mills—research and its practical application. *Powder Technology* 105(1–3), 382–388 (1999).
13. Kwade, A., Schwedes, J.: Breaking characteristics of different materials and their effect on stress intensity and stress number in stirred media mills. *Powder Technology* 122(2–3), 109–121 (2002).
14. Kwade, A.: A stress model for the design of stirred media mills and its application to nanoparticle production. *Chemical Engineering & Technology* 28(7), 718–724 (2005).
15. Breitung-Faes, S., Kwade, A.: Prediction of product size distributions in stirred media mills. *Particuology* 6(4), 321–329 (2008).
16. Stenger, F., Mende, S., Schwedes, J.: Comminution in stirred media mills and nanomaterials production. *Powder Technology* 105(1–3), 333–338 (1999).
17. Mende, S., Stenger, F., Schwedes, J.: Dispersing and grinding of nanoparticles in a stirred media mill. *Chemical Engineering & Technology* 26(3), 341–346 (2003).
18. Fuerstenau, D.W., Abouzeid, A.-Z.M.: The energy efficiency of ball milling in comminution. International Journal of Mineral Processing 67(1-4), 161–185 (2002).
19. Kwade, A., Blecher, L.: Scale-up of stirred media mills. *KONA Powder and Particle Journal* 15, 91–102 (1997).
20. Janković, A., Valery, W., Davis, E.: Cement grinding optimization. *Minerals Engineering* 17(11–12), 1075–1081 (2004).
21. Napier-Munn, T.J., Morrell, S., Morrison, R.D., Kojovic, T.: Mineral Comminution Circuits: Their Operation and Optimisation. JKMRC Monograph Series in Mining and Mineral Processing No. 2, University of Queensland (1996).

22. Cho, H., Kwon, J., Kim, K., Mun, M.: Optimum choice of the make-up ball sizes for maximum throughput in tumbling ball mills. Powder Technology 246, 625–634 (2013).
23. Cundall, P.A., Strack, O.D.L.: A discrete numerical model for granular assemblies. *Géotechnique* 29(1), 47–65 (1979).
24. Tsuji, Y., Kawaguchi, T., Tanaka, T.: Discrete particle simulation of two-dimensional fluidized bed. Powder Technology 77(1), 79–87 (1993).
25. Deen, N.G., van Sint Annaland, M., van der Hoef, M.A., Kuipers, J.A.M.: Review of discrete particle modeling in fluidized beds using the CFDEM method. *Chemical Engineering Science* 62(1–2), 28–44 (2007).
26. Zhu, H.P., Zhou, Z.Y., Yang, R.Y., Yu, A.B.: Discrete particle simulation of particulate systems: a review of major applications and findings. *Chemical Engineering Science* 63(23), 5728–5770 (2008).
27. Cleary, P.W.: Recent advances in DEM modelling of tumbling mills. Minerals Engineering 14(10), 1295–1319 (2001).
28. Sinnott, M.D., Cleary, P.W., Morrison, R.D. (2006). "Analysis of stirred mill performance using DEM simulation: Part 1—Media motion, energy consumption and collisional environment." Minerals Engineering, 19(15), 1537–1550.
29. Sinnott, M.D., Cleary, P.W., Morrison, R.D. (2006). "Analysis of stirred mill performance using DEM simulation: Part 2—Coherent flow structures, liner stress and wear, mixing and transport." Minerals Engineering, 19(15), 1551-1572.
30. Weerasekara, N.S., Powell, M.S., Cole, S., LaRoche, R.D., Favier, J. (2013). "The contribution of DEM to the science of comminution." Powder Technology, 248, 3-24.
31. Powell, M., Smit, I., Radziszewski, P., Cleary, P., Rattray, B., Eriksson, K-G., and Schaeffer, L. (2006). "Selection and design of mill liners." In Advances in Comminution, S. Komar Kawatra, ed., SME, pp. 331-376.
32. Suzzi, D., Radl, S., Khinast, J.G. (2010). "Local analysis of the tablet coating process: Impact of operation conditions on film quality." Chemical Engineering Science, 65(21), 5699-5715.
33. Radeke, C., et al.: Coarse grid CFD–DEM simulation of fluidized beds. *Chemical Engineering Science* 63(21), 5547–5561 (2008).
34. Mori, Y., et al. (2024). "Validation study on a coarse-grained DEM-CFD simulation in a bead mill." Powder Technology, 413, Article 118058.
35. Radl, S., Radeke, C., & Khinast, J.G. (2011). "Parcel-Based Approach for the Simulation of Gas-Particle Flows." 8th International Conference on CFD in Oil & Gas, Metallurgical and Process Industries, Trondheim.
36. Herbst, J.A., & Lichter, J.K. (2006). "Use of multiphysics models for the optimization of comminution operations." In Advances in Comminution, S. Komar Kawatra, ed., SME, pp. 459-478.
37. Sinnott, M.D., Cleary, P.W., Morrison, R.D. (2011). "Slurry flow in a tower mill." Minerals Engineering, 24(3-4), 454-463.
38. Mayank, K., Malahe, M., Govender, I., Mangadoddy, N., 2015, Coupled DEM-CFD Model to Predict the Tumbling Mill Dynamics, Procedia IUTAM, 15, 139-149.
39. Cleary, P.W., Owen, P.: "Effect of particle shape on structure of the charge and nature of energy utilisation in a SAG mill." Minerals Engineering 132, 48-68 (2019).
40. Larsson, S., et al.: A novel DEM/CFD model for stirred media mills predicting power, media and slurry dynamics. *Minerals* 11(1), 55 (2021).
41. Fragnière, G., et al.: Grinding media motion and collisions in stirred media mills using CFD–DEM. *Minerals* 11(2), 185 (2021).

42. Tanneru, Y.S., Finke, J.H., Schilde, C., Harshe, Y.M., Kwade, A.: Coupled CFD-DEM simulation of pin-type wet stirred media mills using immersed boundary approach and hydrodynamic lubrication force. Powder Technology 444, 120060 (2024).
43. Raissi, M., Perdikaris, P., Karniadakis, G.E.: Physics-informed neural networks: A deep learning framework for solving forward and inverse problems involving nonlinear PDEs. *Journal of Computational Physics* 378, 686–707 (2019).
44. Han, J., Jentzen, A., E, W.: Solving high-dimensional partial differential equations using deep learning. *PNAS* 115(34), 8505–8510 (2018).
45. Thuerey, N., Weißenow, K., Prantl, L., Hu, X.: Deep learning methods for Reynolds-averaged Navier–Stokes simulations of airfoil flows. *AIAA Journal* 58(1), 25–36 (2020).
46. Meng, S., Lu, L., Liu, Z., Yao, J., Qin, T., Chen, H., Li, Z.: Machine learning accelerated discrete element modeling of granular flows. Computer Methods in Applied Mechanics and Engineering 369, 113208 (2020).
47. Schmidt, M., Lipson, H.: Distilling free-form natural laws from experimental data. *Science* 324(5923), 81–85 (2009).
48. Cranmer, M.: Interpretable Machine Learning for Science with PySR and SymbolicRegression.jl. arXiv:2305.01582 (2023).
49. Stephens, T.: gplearn: Genetic Programming in Python, with a scikit-learn inspired API. GitHub repository. Available at: https://github.com/trevorstephens/gplearn
50. Tenachi, W., Ibata, R., Diakogiannis, F.I.: Deep symbolic regression for physics guided by units constraints: toward the automated discovery of physical laws. The Astrophysical Journal 959(2), 99 (2023).
51. Hosseinhashemi, S., Zhang, Y., Thon, C., Schilde, C.: Process insights with physics-inspired data-driven modeling- example of battery electrode processing. Journal of Energy Storage 73, 109046 (2023).
52. Kirkpatrick, S., Gelatt, C.D., Vecchi, M.P.: Optimization by simulated annealing. *Science* 220(4598), 671–680 (1983).
53. Černý, V.: Thermodynamical approach to the traveling salesman problem: An efficient simulation algorithm. *Journal of Optimization Theory and Applications* 45(1), 41–51 (1985).
54. Markov, A.A.: Extension of the law of large numbers to dependent quantities. Bulletin of the Physical-Mathematical Society at Kazan University, 2nd series, Volume 15, pp. 135–156 (1906).
55. Harchol-Balter, M.: From Markov Chains to Simple Queues. In: Performance Model-ling and Design of Computer Systems: Queueing Theory in Action, 127–128. Cam-bridge University Press (2013).
56. Liang, F., Liu, C., Carroll, R.J.: Advanced Markov Chain Monte Carlo Methods: Learning from Past Samples. Wiley, Hoboken (2010).
57. Rudin, C.: Stop explaining black box ML models for high-stakes decisions. *Nature Machine Intelligence* 1, 206–215 (2019).
58. Molnar, C.: Interpretable Machine Learning. Independently published (2022).
59. Lipton, Z.C.: The mythos of model interpretability. ACM Queue 16(3), 31–57 (2018).
60. Doshi-Velez, F., Kim, B.: Towards a rigorous science of interpretable ML. *arXiv preprint* arXiv:1702.08608 (2017).
61. Bangi, M.S.F., Kwon, J.S.: Deep hybrid modeling of chemical process: Application to hydraulic fracturing. Computers & Chemical Engineering 134, 106696 (2020).